Mon. Not. R. Astron. Soc. **000**, 1–14 (2012)   Printed 5 March 2013   (MN LaTeX style file v2.2)

arXiv:1205.6203v2 [astro-ph.GA] 16 Jul 2012

The cold veil of the Milky Way stellar halo*

A. J. Deason[1]†, V. Belokurov[1], N. W. Evans[1], S. E. Koposov[1,2], R. J. Cooke[1],
J. Peñarrubia[3], C. F. P. Laporte[1,4], M. Fellhauer[5], M. G. Walker[6], E. W. Olszewski[7]
[1] *Institute of Astronomy, Madingley Rd, Cambridge, CB3 0HA,*
[2] *Sternberg Astronomical Institute, Moscow State University, Universitetskiy pr. 13, Moscow 119991, Russia*
[3] *Ramón y Cajal Fellow, Instituto de Astrofísica de Andalucia-CSIC, Glorieta de la Astronomía s/n, 18008, Granada, Spain*
[4] *Max Planck Institute for Astrophysics, Karl-Schwarzschild Strasse 1, 85740 Garching, Germany,*
[5] *Instituto de Astronomía, Universidad de Concepción, Casilla 160-C, Concpeción, Chile*
[6] *Hubble Fellow, Harvard Smithsonian Center for Astrophysics, 60 Garden Street, Cambridge, MA 02138, USA*
[7] *Steward Observatory, University of Arizona, Tucson, AZ 85721, USA*

June 2012

ABSTRACT

We build a sample of distant ($D > 80$ kpc) stellar halo stars with measured radial velocities. Faint ($20 < g < 22$) candidate blue horizontal branch (BHB) stars were selected using the deep, but wide, multi-epoch Sloan Digital Sky Survey photometry. Follow-up spectroscopy for these A-type stars was performed using the VLT-FORS2 instrument. We classify stars according to their Balmer line profiles, and find 7 are bona fide BHB stars and 31 are blue stragglers (BS). Owing to the magnitude range of our sample, even the intrinsically fainter BS stars can reach out to $D \sim 90$ kpc. We complement this sample of A-type stars with intrinsically brighter, intermediate-age, asymptotic giant branch stars. A set of 4 distant cool carbon stars is compiled from the literature and we perform spectroscopic follow-up on a further 4 N-type carbon stars using the WHT-ISIS instrument. Altogether, this provides us with the largest sample to date of individual star tracers out to $r \sim 150$ kpc. We find that the radial velocity dispersion of these tracers falls rapidly at large distances and is surprisingly cold ($\sigma_r \approx 50-60$ km s^{-1}) between 100-150 kpc. Relating the measured radial velocities to the mass of the Milky Way requires knowledge of the (unknown) tracer density profile and anisotropy at these distances. Nonetheless, by assuming the stellar halo stars between $50-150$ kpc have a moderate density fall-off (with power-law slope $\alpha < 5$) and are on radial orbits ($\sigma_t^2/\sigma_r^2 < 1$), we infer that the mass within 150 kpc is less than $10^{12} M_\odot$ and suggest it probably lies in the range $(5-10) \times 10^{11} M_\odot$. We discuss the implications of such a low mass for the Milky Way.

Key words: Galaxy: fundamental parameters — Galaxy: halo — Galaxy: kinematics and dynamics — stars: blue stragglers — stars: carbon — stars: horizontal branch

1 INTRODUCTION

The formation and evolution of galaxies is fundamentally dependent on their mass. We can measure the mass of a galaxy by a variety of methods. The baryonic component is often inferred by assuming a stellar initial mass function and converting the total integrated starlight into mass. The overall mass, which is dominated by an unseen dark matter component, requires more indirect methods such as gravitational lensing, gas rotation curves, kinematic tracers or timing arguments. Surprisingly, despite being a fundamental parameter, the mass of our own Milky Way Galaxy is poorly known.

The virial mass of the Milky Way has been measured (or inferred) to lie within a large range of values, $5 \times 10^{11} < M_{\rm vir}/M_\odot < 3 \times 10^{12}$. Watkins et al. (2010) found plausible mass estimates in the range $7-34 \times 10^{11} M_\odot$ based on the dynamics of satellite galaxies. This wide range of values partially reflects the unknown properties of the tracer population, but is also caused by a relatively low number of tracers together with uncertainty as to whether some satellites are bound or unbound (e.g. Leo I). Often, total mass estimates are extrapolations from the inner halo to the virial radius. For example, Xue et al. (2008) inferred a virial mass of $1 \times 10^{12} M_\odot$ based on the kinematics of blue horizontal branch (BHB) stars out to 60 kpc. However, it is worth remarking that such an extrapolation leads to a total mass that is not wholly controlled

---

* Based on observations made with ESO Telescopes at the La Silla Paranal Observatory under programme ID 085.B-0567(A) and 088.B-0476(A). Based on observations made with the William Herschel Telescope operated on the island of La Palma by the Isaac Newton Group in the Spanish Observatorio del Roque de los Muchachos of the Instituto de Astrofsica de Canarias.

† E-mail:ajd75,vasily,nwe@ast.cam.ac.uk

© 2012 RAS

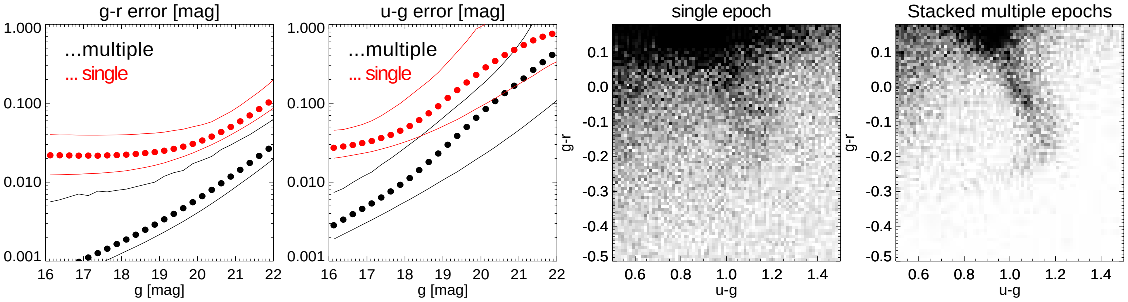

Figure 1. A comparison between single epoch and stacked multiple epoch SDSS stellar photometry. *Left and Middle Left:* Median (dots), 5th and 95th percentiles (solid lines) of the PSF photometric error in the $g-r$ and $u-g$ colour of stars as a function of g band magnitude. *Middle Right and Right:* Density of star-like objects with $16 < g < 23$ in $u-g$, $g-r$ space. The BHB/BS 'claw' is clearly visible in the stacked photometry.

by the data. Obviously, it is preferable to measure the mass out to the virial radius rather than to infer it.

The mass within 50 kpc is constrained by the gas rotation curve (e.g. Rohlfs & Kreitschmann 1988), the orbit of the Magellanic stream (e.g. Besla et al. 2007) and the dynamics of stellar halo stars (e.g. Xue et al. 2008; Gnedin et al. 2010; Samurović & Lalović 2011; Deason et al. 2012). Beyond 50 kpc, we rely on tracers such as satellite galaxies, globular clusters and individual stars. The radial velocity dispersions of these tracer populations provide a direct link to the dark matter, which dominates the gravity field at such distances. In recent years, several studies have shown that velocity dispersions in the Galactic halo begin to decline at distances between $\sim 30-90$ kpc (Battaglia et al. 2005; Brown et al. 2010), perhaps signifying that the 'edge' of the Milky Way is within reach. Battaglia et al. (2005) showed that isothermal mass models predict much flatter velocity dispersion profiles (with $\sigma_r \sim 100$ km s^{-1}) than observed. However, despite recent discoveries with Sloan Digital Sky Survey (SDSS) imaging (e.g. Belokurov et al. 2007), there are unfortunately few known satellite galaxies and globular clusters at distances beyond 80 kpc, which is where most of the mass uncertainty now arises. Thus, our knowledge of the Milky Way's *total* mass is limited by the availability of dynamical tracers at large distances.

The best way of overcoming the paucity of objects is to use distant halo stars as tracers. This has the advantage that there are many more of them than satellite galaxies. Of halo stars, BHBs are attractive targets because there exist well-understood methods for their selection using colour-colour diagrams (e.g. Sirko et al. 2004), as well as algorithms for removal of the principal contaminants like blue stragglers (BS) (e.g. Clewley et al. 2002). The SDSS itself takes advantage of the efficiency of the method and today has already acquired spectra of thousands of BHBs over 1/4 of the sky (Xue et al. 2008; Deason et al. 2011a; Xue et al. 2011). These stars are however typically brighter than 19.5 magnitudes, and therefore at best can reach 60 kpc (see e.g., Xue et al. 2008). Studies such as those pioneered by Clewley et al. (2002) go deeper, but are limited to small areas of the sky, and hence are susceptible to effects such as substructure (Clewley et al. 2005). In this work, we go both deeper and wider by making use of multi-epoch SDSS photometry to select distant BHB candidate stars.

We target distant BHB stars in the magnitude range $20 < g < 22$ (or a distance range of $80 < D/\mathrm{kpc} < 200$ for BHBs) for spectroscopic follow-up. These faint candidates require large 8-10m class telescopes – such as the European Southern Observatory (ESO) Very Large Telescope (VLT) facility – to obtain sufficient signal-to-noise ratio (S/N) to classify the stars and measure their radial velocities. We complement this sample of relatively old stars with intermediate-age, asymptotic giant branch (AGB) stars. In particular, we compile a sample of distant N type carbon (CN) stars, which are bright ($M_{\rm R} \sim -3.5$) and can be detected out to extremely large distances. In fact, their radial velocities can comfortably be measured with 4m class telescopes such as the William Herschel Telescope (WHT). In addition, unlike other AGB giant stars, they can be cleanly selected using infrared photometry with little contamination from dwarf stars (Totten & Irwin 1998; Totten et al. 2000). While these CN stars suffer less from photometric contamination than BHB stars, they are intrinsically rare and many (within <100 kpc) belong to the Sagittarius stream (Ibata et al. 2001; Mauron et al. 2004). However, by constructing distant halo samples of both populations we can ensure that our results are not subject to a particular stellar type.

The paper is arranged as follows. In Section 2, we outline our target selection process and VLT-FORS2 spectroscopic follow-up programme for candidate distant A-type stars. In addition, we outline the classification of our targets as BHB or BS stars based on their Balmer line profiles and assign distances according to this classification. In Section 3, we compile a sample of distant CN type stars in the literature with measured radial velocities. We perform spectroscopic follow-up of a further four stars using the WHT-ISIS instrument. We address the possibility that our distant stellar halo stars belong to substructure in Section 4. The velocity dispersion profile of our sample of distant stellar halo stars is analysed in Section 5 and we consider the implications for the mass of the Milky Way in Section 6, and sum up in Section 7.

2 A-TYPE STARS

We aim to measure radial velocities of distant ($D > 80$ kpc) BHB stars. Selecting potential BHB candidates at such faint magnitudes ($20 < g < 22$) requires deep and accurate photometry. This is especially important in the u band, which gives the most discriminating power between BHB and BS stars (Deason et al. 2011b). A wide sky coverage is also beneficial to avoid targeting possible substructures. Unfortunately, these two requirements are often mutually exclusive with wider surveys having shallower photometry than deeper pencil beam surveys. We have overcome this problem by making use of the SDSS multi-epoch photometry. The deeper photometry provided by stacking multi-epoch data allows us to target distant BHB stars over a wide sky area. In the following sub-sections, we outline our target selection and follow-up spectroscopic programme.

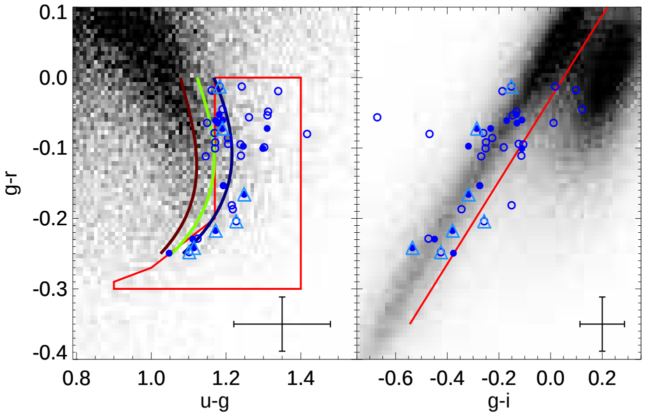

Figure 2. *Left panel:* The density of stars with $19 < g < 22$ in $u-g, g-r$ colour-colour space with stacked multi-epoch ($N_{\rm overlaps} > 2$) photometry. The red region shows the BHB star selection box. The BHB/BS star ridgelines (cf. Deason et al. 2011b) and approximate dividing line between the two populations are shown by the blue/red and green lines respectively. Stars selected for the P85 and P88 observations are shown by the open/filled blue symbols. The typical error of these points is shown in the bottom right corner. The light blue triangles around symbols indicate stars that are classified as BHBs in Section 2.3. *Right:* The density of stars in $g-r$, $g-i$ colour space. QSOs occupy the upper right hand region of this plot. The red line indicates the divide between QSOs and stars. Note that this cut was not applied in the P85 observations.

2.1 Target Selection

We have used deep photometry obtained by stacking multiple exposures in the SDSS Stripe 82 to select faint BHB candidates with robust colour measurements. Stripe 82 is a 2.5 degrees wide stripe that runs at constant DEC $= 0$ deg and $-60 < \mathrm{RA/deg} < 60$. During the SDSS Supernova search programme, locations along the Stripe were imaged 20-50 times during the years 2000-2007. Individual Stripe 82 images were stacked to produce deeper master frames, which give a final catalogue of u, g, r, i, z measurements for stars and galaxies that is complete to 1-2 magnitudes fainter than that of SDSS single-epoch observations. The left and middle left panels of Fig. 1 illustrate the improved precision in $g-r$ and $u-g$ for star-like objects in the stacked Stripe 82 data. The middle right and right panel of Fig. 1 show the overall effect of obtaining deeper photometry around the BHB locus.

We have supplemented our BHB candidates selected from Stripe 82 with a further sample chosen from the remaining overlaps in the SDSS 8th data release sky coverage. About 40 per cent of the SDSS field of view is observed more than once, as the survey stripes overlap. Typically, the overlaps are observed at least twice, and occasionally 3-4 times. While shallower than Stripe 82 data, these multi-epoch data improve the precision of magnitudes measured for faint candidates. We select stellar objects with clean photometry, which have had 3 or more detections within 0.5 arcseconds. For each object, we combine the measurements from different observing runs and calculate average u, g, r magnitudes together with the scatter in each band (removing those with standard deviations greater than 0.5 mag in each band). The wider coverage of these SDSS overlaps allows us to complement the deep photometry in Stripe 82 with a broader field of view.

This multi-epoch SDSS photometry allows us to easily identify A-type stars which occupy the 'claw' in $u-g$, $g-r$ colour space; the locus of BHB stars is slightly redder in $u-g$ than BS stars (Deason et al. 2011b). We define the following selection box to maximise the number of BHB targets:

$$
\begin{aligned}
(u-g)_{\rm BHB} &= [1.17, 1.17, 1.0, 0.9, 0.9, 1.4, 1.4, 1.17] \qquad (1)\\
(g-r)_{\rm BHB} &= [0, -0.2, -0.27, -0.29, -0.3, -0.3, 0, 0]
\end{aligned}
$$

Stars in the magnitude range, $20 < g < 22$, that lie within this colour-colour box, are identified as candidate distant BHB stars. Even at brighter magnitudes, there is significant overlap between the BHB and BS populations in $u-g$, $g-r$ colour-colour space and so we expect there to be significant contamination by BS stars in our selected targets. In particular, the relatively large errors in $u-g$ (see error bar in left panel of Fig. 2) means that there can be significant scatter from BS stars into the BHB selection region. However, we note that at such faint magnitudes ($g > 20$), even BS stars can probe out to relatively large distances ($D \leqslant 90$ kpc).

In Fig. 2, we show the targets selected for spectroscopic follow-up. Stars observed in our first (P85) and second (P88) observing runs are shown by the unfilled and filled circles respectively. For the second run, we applied an extra cut in $g-r$, $g-i$ space as shown in the right-hand panel of Fig. 2. By excluding stars in the upper right region of this plot, we avoid contamination from quasi-stellar objects (QSOs) in our sample.

2.2 VLT-FORS2 follow-up spectroscopy

We used the VLT FORS2 instrument (in service mode) to obtain low resolution ($R \sim 800$) optical spectra of the 48 BHB candidates. Observations were made in long-slit spectroscopy mode with a 1.0 arcsec slit. We used the 600B grism giving a dispersion of 1.2Å per pixel. The spectral coverage, $\lambda = 3400-6100$Å includes the Balmer lines Hδ, Hγ and Hβ. Observations were taken in 2010 April-August (P85) and 2011-12 October-February (P88). For stars in the magnitude range $20 < g < 22$, we required integration times between 20 minutes and 2 hours to achieve a S/N ratio of 10 per resolution element.

The spectroscopic data were reduced using the ESOREX pipeline provided by ESO. This pipeline performs all of the necessary steps for reducing our science frames, including bias subtraction, flat-fielding, spectral extraction and sky subtraction. A wavelength calibration was applied with reference to HgCdHe arc lamp observations. By comparing our wavelength solution to strong sky lines (e.g. OI λ5577Å), we were able to make fine corrections to the wavelength solution if necessary. The uncertainty in the wavelength solution (typically 6 km s^{-1}) is propagated forward into our velocity errors. Finally, the data were flux-calibrated with reference to standard star observations.

From an inspection of the reduced spectra, we identified 4 targets as QSOs and 1 target was too faint to be extracted. Thus, our sample contains 43 A-type stars.

2.3 BHB/BS Classification

2.3.1 *Template spectra*

To classify our A-type stars, we construct a sample of BHB and BS template spectra using high S/N SDSS DR7 data. To select A-type stars, we impose constraints on the (extinction corrected) $u-g$ and $g-r$ colours, the surface gravity (g_s) and the effective temperature ($T_{\rm eff}$), namely:

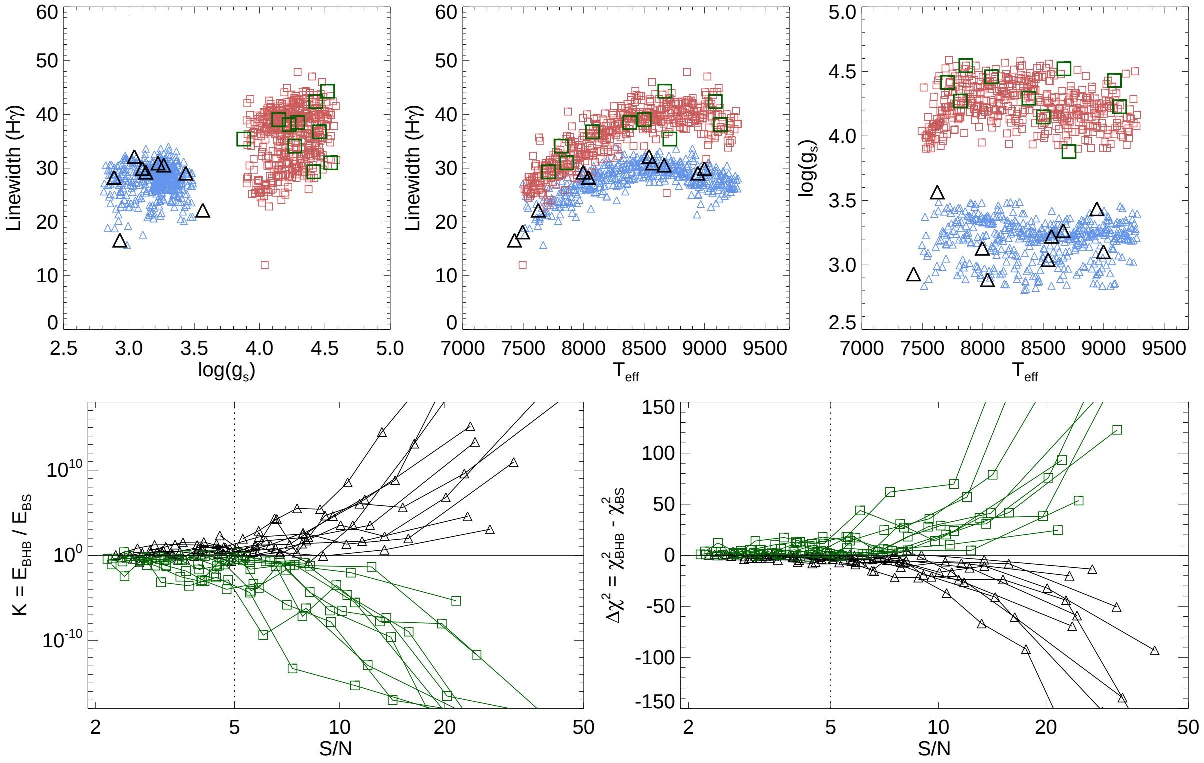

Figure 3. Top panels: Properties of our SDSS template spectra. We show the Hγ linewidths (similar trends are seen for Hδ and Hβ), effective temperature and surface gravity. The blue triangles are the BHB templates and the red squares are the BS templates. We select 10 BHB and 10 BS test samples which are not in our template library. These are shown by the green squares (BS) and black triangles (BHB). Bottom panels: We degrade the S/N of the test samples and apply our template fitting routine. The left panel shows the Bayes factor (ratio of evidences) as a function of S/N. Stars with $K > 1$ are classified as BHB stars. Below S/N < 5 the stars become more difficult to classify. In the right hand panel, we show the difference between the minimum Chi-square values for the BHB and BS templates. BHB stars have negative $\Delta\chi^2$ values.

$$\begin{aligned} 0.7 < u-g < 1.4 \\ -0.3 < g-r < 0 \\ 2.8 < \log(g_s) < 4.6 \\ 7500 < T_{\rm eff}/{\rm K} < 9300 \end{aligned} \qquad (2)$$

At high S/N, BHB and BS stars can be classified according to their surface gravity. The boundary between the two populations lies at $\log(g_s) = 3.5 - 4.0$. We select 1000 of these A-type stars with high S/N (> 20) that are approximately uniform in $\log(g)$-$T_{\rm eff}$ space and we exclude borderline cases ($3.5 < \log(g_s) < 4$, this excludes < 10 per cent of each population). This sample is roughly evenly split between BHB and BS stars. The top right hand panel of Fig. 3 shows the surface gravity and effective temperature distribution of the BHB (blue triangles) and BS (red squares) stars.

To construct templates from this sample, we parametrise the spectra in the wavelength range $4000 < \lambda/\text{Å} < 5000$. This spans the wavelength coverage of our VLT-FORS2 sample and includes the Balmer lines Hδ, Hγ and Hβ. We normalise the spectra by fitting a polynomial of order 5 to the continuum flux distribution, thus excluding regions that are affected by absorption lines. We adopt the Sersic (1968) function to fit the absorption line profiles of the normalised spectra:

$$y = 1.0 - a \exp\left[-\left(\frac{|x - x_0|}{b}\right)^c\right] \qquad (3)$$

The parameters x_0 and a give the wavelength and line depth at the line centre respectively. The parameter b provides a measure of the linewidth and the parameter c quantifies the line shape. The model profiles are convolved with the full-width at half-maximum (FWHM) resolution ($\sim$ 2.3 Å) of the SDSS spectra. Our profiles are fitted using the publicly available IDL MPFIT[1] programme (Markwardt 2009).

Thus, each A-type 'template' star is parametrised by the (5th order polynomial) continuum and the Sersic profiles of the Hδ, Hγ and Hβ Balmer lines. This parametrisation is used to produce noise-free templates. The Sersic profile parameters and continuum shape of the stars are governed by their surface gravity and effective temperature. Thus, when fitting the data, we vary the template ID, which is equivalent to varying $\log(g_s)$ and $T_{\rm eff}$. In the top panels of Fig. 3, we show the Hγ linewidths, effective temperature and surface gravity for our template stars.

Each of these template stars is a model to which we can compare our VLT-FORS2 data. The models are convolved with the FWHM resolution applicable to our VLT-FORS2 observations ($\sim$ 4 Å), where we measure the FWHM from the arc lines. For each model, there are two free parameters; the velocity and a constant scale factor. **The derived velocities are based solely on the three strong Balmer lines, and both BHB and BS template fits give**

---

[1] http://purl.com/net/mpfit

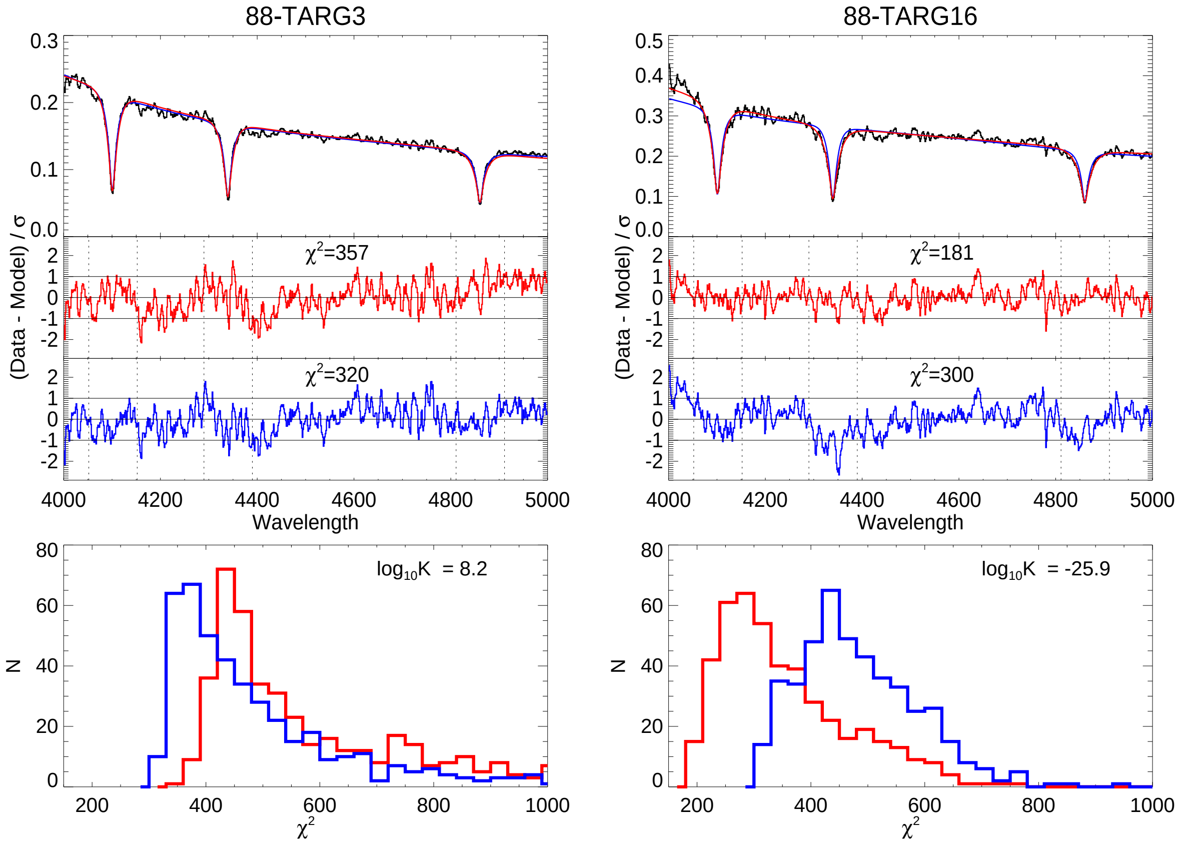

Figure 4. Top panels: We show the minimum Chi-square template fits for two stars in our VLT-FORS2 sample. The residuals for the corresponding best-fit BHB (blue line) and BS (red line) templates are also shown. The dotted lines indicate the regions where the Chi square values are evaluated; these are centred on the three Balmer lines. Bottom panels: For the same two stars, we show the distribution of Chi-square values for all of the BHB and BS templates. The two stars (88-TARG3 and 88-TARG16) can be cleanly classified as a BHB or BS.

very similar velocities. The Chi-square value of each fit can then be used to decide if BHB star templates or BS star templates provide a better description of the data. To statistically determine the preferred model type, we use the ratio of evidences (or the Bayes factor):

$$
\begin{aligned}
K &= \frac{E_{\rm BHB}}{E_{\rm BS}} = \frac{\int {\rm Prior}(\theta_{\rm BHB}) \exp\left(-\chi^2(\theta_{\rm BHB})/2\right)\, {\rm d}\theta_{\rm BHB}}{\int {\rm Prior}(\theta_{\rm BS}) \exp\left(-\chi^2(\theta_{\rm BS})/2\right)\, {\rm d}\theta_{\rm BS}} \qquad (4)\\
&\simeq \frac{\sum_i {\rm Prior}(\psi)_{\rm BHB,i} \sqrt{|{\rm Cov}(\psi)|_{\rm BHB,i}} \exp\left(-\chi^2_{\rm BHB,i}/2\right)}{\sum_i {\rm Prior}(\psi)_{\rm BS,i} \sqrt{|{\rm Cov}(\psi)|_{\rm BS,i}} \exp\left(-\chi^2_{\rm BS,i}/2\right)}
\end{aligned}
$$

Here, θ denotes the parameter space over which the template models span; the template IDs (which cover a range of surface gravities and effective temperatures) and the free parameters in each template fit. The sum is performed over all templates, where ψ denotes the two free parameters for each template fit, $v_{\rm los}$ and a constant scale factor. A Gaussian approximation is assumed for the marginalisation over the ψ parameters, which then depends on the corresponding covariance matrix ($|{\rm Cov}(\psi)|$, see e.g. MacKay 2003). We assume uniform priors for all parameters except the constant scale factor, for which we use a Jeffrey's scale invariant prior (Jeffreys 1961).

Equation 4 gives the ratio of marginalised likelihoods. However, we can compute the *posterior* odds by multiplying the likelihood ratio by the prior odds. In our case, the prior odds could be the number ratio of BHB-to-BS stars, i.e. $\tilde{K} = (f_{\rm BHB}/f_{\rm BS})\, K$. In most cases, we do not know the number ratio of BHB-to-BS stars prior and by assuming $f_{\rm BHB} = f_{\rm BS}$, the prior evidence ratio reduces to $\tilde{K} = K$.

We test our method of classifying BHB and BS stars by randomly selecting 10 BHB and 10 BS stars from the SDSS sample. These stars are not included in our template spectra sample. They are shown by the black triangles (BHB) and green squares (BS) in Fig. 3. We perform our fitting routine on these test cases and vary the S/N by degrading the spectra. The results of this exercise are illustrated in the bottom panels of Fig. 3. In the left panel, we show the Bayes factor, K, as a function of S/N. The right panel shows the difference in Chi-square values between the best fitting BHB and BS models. The BHB stars should have $K > 1$ and $\Delta\chi^2 < 0$. At S/N > 5, the classification is almost always correct ($> 90\%$) and stars can easily be classified when S/N > 10. However, we find that below S/N < 5, the stars become more difficult to classify.

We observed three 'standard' BHB stars over our observing run. These are bright ($V \sim 15$) stars classified as BHBs in the literature. Two of these stars were observed in P85 and reside in the M5 globular cluster (cf. Clewley et al. 2002) and one is taken from the Xue et al. (2008) sample of SDSS BHB stars and was observed in P88. We applied the same data reduction procedures to these standard stars as our main sample. We apply our template fitting technique to these stars and obtain very high evidence ratios ($\log_{10} K > 100$), as expected for such high S/N spectra (S/N ~ 100).

ID	ra [deg]	dec [deg]	$g_{\rm mag}$	(S/N) pix^{-1}	$\chi^2_{\rm BHB}$	$\chi^2_{\rm BS}$	$\log_{10} K$	$\log_{10} \tilde{K}$	$T_{\rm eff}$ K	$\log(g_s)$	$V_{\rm hel}$ km s^{-1}	D kpc	Class
85-TARG2	219.2258	0.8461	21.8	6.4	262.7	235.9	-5.87	-6.60	8529	4.31	-38 ± 23	72 ± 17	BS
85-TARG3	220.6565	-1.1907	21.7	6.3	268.9	254.4	-3.17	-3.90	8286	4.32	86 ± 21	60 ± 14	BS
85-TARG4	202.4456	8.3195	21.5	10.1	311.3	305.4	-1.25	-1.98	7568	4.04	8 ± 13	55 ± 13	BS
85-TARG5	217.5596	7.3932	21.5	9.8	338.3	323.3	-3.32	-4.05	7614	4.08	-73 ± 20	59 ± 14	BS
85-TARG7	204.0844	4.7730	21.5	10.3	405.6	397.0	-1.84	-2.57	7578	4.05	64 ± 21	62 ± 14	BS
85-TARG10	204.9583	3.3285	21.1	8.2	348.6	341.7	-2.06	-2.78	7851	4.52	93 ± 28	54 ± 13	BS
85-TARG12	226.0665	3.1375	21.0	10.5	281.4	266.7	-3.25	-3.97	8286	4.32	6 ± 20	54 ± 12	BS
85-TARG13	233.7010	-0.8291	21.0	11.0	363.8	300.0	-13.92	-14.65	9182	4.48	116 ± 18	48 ± 11	BS
85-TARG15	151.2014	11.7011	21.2	4.9	199.6	191.9	-1.79	-2.52	7614	4.08	67 ± 28	71 ± 16	BS
85-TARG17	192.8952	6.2015	20.9	7.6	255.1	247.7	-1.94	-2.67	8286	4.32	278 ± 24	46 ± 11	BS
85-TARG18	200.6029	10.8438	21.2	9.1	341.4	330.3	-1.94	-2.66	7614	4.08	137 ± 37	53 ± 12	BS
85-TARG20	227.1404	-0.8308	20.5	8.7	370.5	299.7	-15.45	-16.18	8013	4.27	142 ± 36	40 ± 9	BS
85-TARG21	203.6062	3.4247	20.8	6.7	221.2	209.4	-2.95	-3.67	8675	4.18	15 ± 28	50 ± 12	BS
85-TARG23	138.2685	2.7640	20.8	7.6	274.4	259.2	-3.71	-4.44	8499	4.14	305 ± 36	48 ± 11	BS
85-TARG24	203.2243	5.1525	20.5	4.1	442.7	260.2	-39.81	-40.53	8437	4.44	25 ± 13	55 ± 13	BS
85-TARG33	206.9920	-1.1284	20.3	16.9	279.1	285.4	2.17	1.44	8406	3.27	2 ± 20	83 ± 4	BHB
85-TARG34	133.3904	-0.3267	20.3	6.3	213.5	221.9	2.54	1.81	8477	3.21	131 ± 18	88 ± 4	BHB
85-TARG36	204.1527	5.6618	20.3	3.8	350.7	331.6	-4.19	-4.92	7614	4.08	34 ± 19	32 ± 7	BS
85-TARG38	179.1346	6.6239	20.3	4.7	354.9	280.8	-16.17	-16.90	8494	4.47	37 ± 16	39 ± 9	BS
88-TARG2	45.0211	-0.3606	20.8	14.8	356.6	299.1	-12.65	-13.38	8708	4.06	164 ± 13	65 ± 15	BS
88-TARG3	28.1598	0.0305	21.0	12.1	320.1	357.1	8.16	7.43	8700	3.07	-73 ± 10	119 ± 6	BHB
88-TARG4	23.7335	0.9832	21.0	14.6	414.6	353.2	-13.49	-14.22	8442	4.47	-181 ± 15	52 ± 12	BS
88-TARG5	27.1481	0.6968	21.3	18.7	348.4	315.5	-7.25	-7.97	9074	4.36	-11 ± 38	86 ± 20	BS
88-TARG7	12.6871	13.9173	21.0	14.7	283.6	292.9	2.32	1.59	8801	3.28	-121 ± 13	116 ± 5	BHB
88-TARG8	22.4696	3.2119	21.1	11.5	282.0	289.9	1.68	0.96	8795	3.32	-47 ± 14	133 ± 6	BHB
88-TARG9	10.3506	0.1664	20.8	16.0	334.1	333.1	-0.47	-1.20	8529	4.31	-129 ± 35	54 ± 12	BS(?)
88-TARG15	42.0548	-6.8055	20.6	10.8	351.8	278.7	-15.89	-16.62	8442	4.47	-52 ± 15	43 ± 10	BS
88-TARG16	65.2176	-0.6718	20.2	10.5	300.2	181.2	-25.86	-26.59	9074	4.36	-69 ± 17	44 ± 10	BS
88-TARG32	16.4854	-1.2477	21.2	16.9	351.4	272.7	-17.15	-17.87	8442	4.47	-11 ± 19	56 ± 13	BS
88-TARG33	50.1435	-0.7992	21.0	14.4	381.7	312.2	-15.11	-15.84	8442	4.47	-100 ± 16	49 ± 11	BS
88-TARG34	4.4821	0.0631	21.3	12.8	165.3	172.5	1.41	0.68	8233	3.24	-88 ± 16	151 ± 7	BHB
88-TARG35	23.7335	0.9831	21.0	16.5	361.9	234.4	-27.88	-28.61	8297	4.45	-173 ± 12	48 ± 11	BS
88-TARG36	20.7336	-0.6500	21.2	20.5	298.3	270.6	-6.38	-7.11	8175	4.35	-36 ± 14	53 ± 12	BS
88-TARG37	1.5332	-0.2538	21.3	11.8	333.6	291.6	-9.13	-9.86	8297	4.45	-363 ± 19	54 ± 12	BS
88-TARG41	41.3665	-9.0043	20.8	11.6	210.1	186.3	-5.27	-6.00	9182	4.48	-78 ± 26	49 ± 11	BS
88-TARG100	49.0847	-0.1127	20.8	11.6	269.9	272.5	0.50	-0.23	7522	3.37	-35 ± 13	117 ± 5	BHB(?)
88-TARG105	40.9579	-0.6469	20.2	14.1	197.4	192.6	-1.36	-2.09	7959	4.23	34 ± 18	35 ± 8	BS
88-TARG110	49.0308	-0.5904	20.0	14.2	363.5	310.1	-11.77	-12.49	8297	4.45	-75 ± 13	33 ± 8	BS

Table 1. We list the classifiable A-type stars observed in our VLT run. The columns list the ID, the right ascension and declination, the (extinction corrected) magnitude, the S/N per resolution element, the *minimum* Chi-square value for the BHB and BS star templates, the ratio of the BHB and BS evidences (K), the evidence ratio weighted by the fraction of BHB-to-BS star priors ($\tilde{K}$), the effective temperature and surface gravity of the best fitting template model, the observed heliocentric velocities, and the distance derived from the $g-r$ colours according to the stellar classification (i.e. BHB or BS). The final column gives the assigned classification with a question mark indicating borderline cases.

2.3.2 Results

A small number (5) of our VLT-FORS sample are too noisy to classify (S/N < 5) and so we apply our fitting method to the remaining (38) classifiable A-type stars. The results are summarised in Table 1, where we give the measured heliocentric velocity and final classification for each star. We show an example of a BHB (88-TARG3, left column) and a BS (88-TARG16, right column) star in Fig. 4. The top panels show the spectrum (black line) and the best fitting BHB (blue line) and BS (red line) models overplotted. The residuals for each fit are also shown. The bottom panels show the distribution of χ^2 values for each template fit. In these two cases, the stars are easily identified as a BHB or BS.

We classify stars with $K > 1$ as BHB stars. This classification method identifies 7 BHB stars and 31 BS stars. Jeffreys (1961) define $K > 3$ or $K < 1/3$ as substantial evidence for (or against) a particular model. Following this interpretation, two of our stars (88-TARG100 and 88-TARG9) are identified as borderline cases. While we do not have prior knowledge of the fraction of BHB and BS stars, we can iteratively compute $\tilde{K}$. We begin by assuming $f_{\mathrm{BHB}} = 0.5$ and then iterate until the fraction of BHB stars converges (to $f_{\mathrm{BHB}} = 0.16$). The low fraction of BHB stars means that $\tilde{K} < K$ and in one borderline case (88-TARG100) $K > 1$, but including the prior factor gives $\tilde{K} < 1$.

2.4 Distances

BHB stars are near ideal ‘standard candles’ owing to their intrinsic brightness and narrow range of absolute magnitudes. However, BS stars are fainter (by ~ 2 mags) and have a much larger range of intrinsic luminosities. We assign absolute magnitudes to the two populations using the absolute magnitude-colour relations given by equation 7 in Deason et al. (2011b). The spread in absolute magnitude about this relation is fairly narrow for BHBs ($\Delta M_g \sim 0.15$) as compared to BS stars ($\Delta M_g \sim 0.5$). Heliocentric distances are assigned to our A-type stars according to their classification as a BHB or BS star. The BS stars span a distance range $30 < D/\mathrm{kpc} < 90$, whilst the BHB stars probe much further distances $80 < D/\mathrm{kpc} < 150$.

3 COOL CARBON STARS

We complement our sample of A-type stars with distant ($D > 80$ kpc) cool carbon stars, which have radial velocities published in the literature. In particular, we focus on N-type carbon (CN) stars owing to their clean photometric selection using JHK bands and their bright intrinsic luminosity (see e.g. Totten & Irwin 1998); CN stars with apparent magnitudes as bright as $r \sim 15$ can reach out to $D \sim 80-100$ kpc. In addition to the literature sample of CN stars (with details provided in table 2), we obtain follow-up spectroscopy for four CN stars which do not have radial velocity measurements. We outline their selection and follow-up spectroscopy below.

We target CN stars using SDSS optical photometry and Two Micron All Sky Survey (2MASS) or UKIRT Infrared Deep Sky Survey (UKIDSS) infrared photometry. We select SDSS stars with very red colours ($g-r > 1.75$) and with no appreciable proper motion ($\mu < 9$ mas yr^{-1}). These stars are then cross-matched with the infrared catalogues to obtain their JHK magnitudes. In Fig. 5, we show the resulting candidates from UKIDSS photometry by the black dots. The CN-type, CH-type and dwarf star classification boundaries are shown by the dotted lines (see Totten et al. 2000). The CH-type stars and dwarfs stars greatly outnumber the CN type stars. This is unsurprising given that the CN type stars are intrinsically rare (Totten & Irwin 1998) and also probe much greater distances. The purple crosses show the distant CN stars given in Table 2. The circles indicate stars without radial velocity measurements for which we perform follow-up spectroscopy. Two of these stars are selected from cross-matching SDSS with either 2MASS or UKIDSS photometry. The remaining two are classified as CN stars by Mauron (2008) and have estimated distances $D > 100$ kpc.

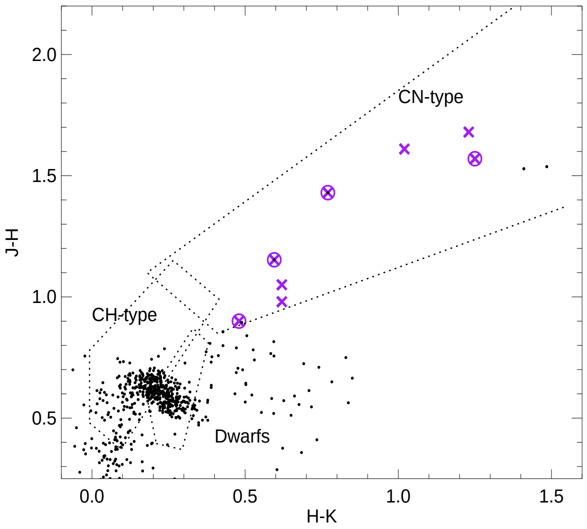

Figure 5. $J-H$, $H-K$ colours of very red ($g-r > 1.75$) SDSS stars with small proper motion ($\mu < 9$ mas yr^{-1}) cross-matched with UKIDSS stars. The classification boundaries for CH, CN and dwarf stars are taken from Totten et al. (2000). The purple crosses show the distant CN stars given in Table 2. The circled indicate stars for which we perform follow-up spectroscopy.

3.1 WHT-ISIS follow-up Spectroscopy

We used the WHT ISIS instrument to obtain high resolution ($R \sim 5000$) optical spectra of the 4 CN type stars. Long slit spectroscopic observations were made in good conditions (seeing ~ 1.0 arcsec) with a 0.8 arcsec wide slit. We used the R1200 grating giving a dispersion of 0.26Å per pixel. The spectral coverage, $\lambda \simeq 7500-8500$Å, includes several CN absorption bands. These observations were taken on 2012 March 27-31. For stars in the magnitude range $15 < r < 19$, we required integration times between 300 seconds and 1 hour to achieve a S/N ratio of 10 per resolution element. We follow the data reduction procedure outlined in Totten & Irwin (1998). In short, the spectroscopic data were reduced using the standard IRAF software packages. First, the science frames were bias subtracted and flat-fielded. Background regions were selected for sky subtraction during the extraction of the science data. The extracted stellar spectra were wavelength calibrated with reference to CuNe+CuAr arc lamp observations. As a final step, the reduced data were flux calibrated with observations of flux standard stars.

We also observed several carbon star radial velocity standards. These stars were observed and reduced with identical instrument setup and data reduction procedures as described above for our science targets. We use these standard stars as templates to determine

ID	RA (J2000) [deg]	DEC (J2000) [deg]	$J_{\rm mag}$	$H_{\rm mag}$	$K_{\rm mag}$	$V_{\rm hel}$ km s^{-1}	$D_{\rm M}$ kpc	$D_{\rm TI}$ kpc	Ref.
B1429-0518	218.1198	-5.5216	13.9	12.3	11.0	77 ± 6	70	94	TI98/00
B1450-1300	223.4304	-13.2180	13.9	12.3	11.3	120 ± 5	76	101	TI98/00
J2246-2726	341.6206	-27.4501	14.9	13.9	13.3	2 ± 10	130	160	M05
J1141-3341	175.4258	-33.6928	13.9	12.8	12.2	144 ± 10	82	102	M05
J1446-0055	221.6295	-0.9168	13.6	12.2	11.4	15 ± 10	71	95	UKIDSS-ISIS
J1301+0029	195.3269	0.4975	14.9	13.7	13.1	61 ± 10	153	169	UKIDSS/M08-ISIS
J1725+0300	261.4764	3.0072	14.8	13.9	13.4	-72 ± 10	115	136	M08-ISIS
J0905+2025	136.4432	20.4106	15.1	13.6	12.3	200 ± 10	140	165	2MASS-ISIS

Table 2. We list the distant CN stars with radial velocities from the literature or velocities measured in this work. The columns give the ID, the right ascension and declination, the infrared J, H and K magnitudes, the observed heliocentric velocities and the estimated distances using the Mauron et al. (2004) prescription or the Totten et al. (2000) relation. We adopt the mean of these distances with an associated distance error of 25 per cent. The final column lists the reference for the photometry and measured velocities: Mauron et al. 2005 (M05); Mauron 2008 (M08); Totten & Irwin 1998 (TI98); Totten et al. 2000 (TI00).

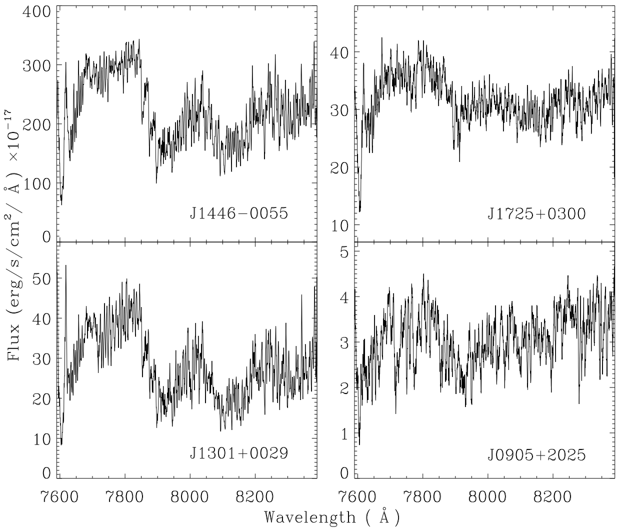

Figure 6. High resolution spectra for the four CN-type stars. We concentrate on the wavelength region $7500 < \lambda$/Å< 8500 where there are several CN absorption bands. The apparent 'noisiness' of the data is due to the many CN absorption lines, and not entirely due to photon counting errors.

the velocities of our science targets using cross-correlation techniques. With the high resolution and modest signal-to-noise of the data (S/N $\sim$ 10), the near-infrared CN absorption bands are well defined and lead to good-quality cross-correlation peaks. There are several velocity errors that affect the final results including wavelength calibration uncertainties, mismatched template versus science target stars and random errors due to photon counting. The combined effect of all these errors gives velocity uncertainties of $\sim$ 10 km s^{-1}.

3.2 Distances

We assign distances to the carbon stars using their K band magnitude. We use infrared rather than optical photometry, since the former is more robust to extinction and variability effects. Totten et al. (2000) estimated distances to CN type carbon stars by calibrating against Galactic satellites. This calibration is largely dominated by stars belonging to the Large Magellanic Cloud (LMC) and Small Magellanic Cloud (SMC). Mauron et al. (2004) use carbon stars in Sagittarius (Sgr) to assign distances to their stars. The authors note that the carbon stars of Sgr are less luminous by ~ 0.5 mag in the K band than the Carbon stars in the LMC. Thus, the distances derived by Mauron et al. (2004) are ~ 25 percent closer than those derived by Totten et al. (2000). In Table 2, we give both the Totten et al. (2000) ($D_{\rm TI}$) and Mauron et al. (2004) ($D_{\rm M}$) distances of our CN type stars. We adopt the mean of these two distances in this work and assume errors of $\sigma_D \sim 25$ percent.

Our final sample consists of 8 CN type stars in the distance range $80 < D/{\rm kpc} < 160$, 7 BHB stars with $80 < D/{\rm kpc} < 150$ and 31 BS stars with $30 < D/{\rm kpc} < 90$. This is the largest sample of distant stellar halo stars with measured radial velocities to date.

4 FIELD STARS OR SUBSTRUCTURE?

In this section, we look at the distribution of our halo stars in both position and (line-of-sight) velocity space. We convert our observed heliocentric velocities to a Galactocentric frame by assuming a circular speed[2] of 240 km s^{-1} (recently revised upwards, see Reid et al. 2009, Bovy et al. 2009, McMillan 2011 and Deason et al. 2011a) at the position of the Sun ($R_0 = 8.5$ kpc) with a solar peculiar motion (U, V, W) = (11.1, 12.24, 7.25) km s^{-1} (Schönrich et al. 2010).

Fig. 7 plots the positions of our distant halo stars on the sky. The top panel shows the right ascension (RA), declination (DEC) distribution (in J2000) and the middle and bottom panels show distance and Galactocentric velocity as a function of right ascension. Our 7 BHB stars are widely distributed over the sky and show no signs of clustering. The BS stars (and some CN type stars), however, do show signs of sharing common position and velocity features. The black lines depict the approximate tracks in position and

---

[2] **We ensured that our results are not strongly affected by our choice of the solar reflex motion. Our main results are unchanged if we adopt values in the range 180-280 km s^{-1}.**

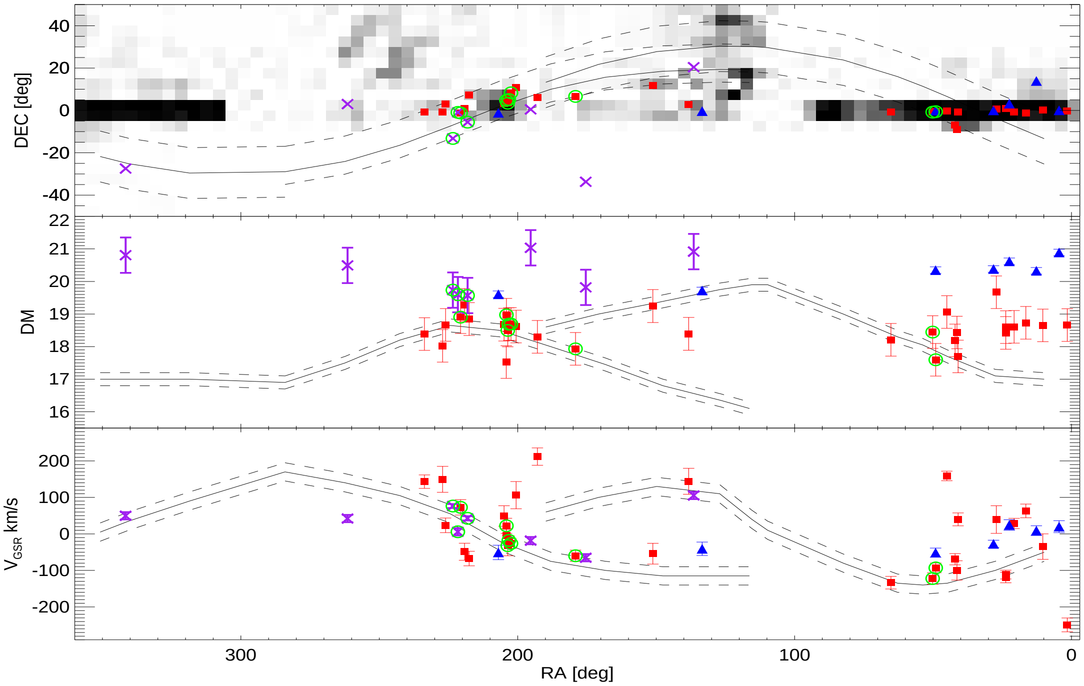

Figure 7. *Top panel:* The distribution of our A-type and CN-type stars on the sky. The red squares, blue triangles and purple crosses indicate BS, BHB and CN stars respectively. The shaded regions show the density of stars which have multi-epoch photometry ($N_{\rm overlap} > 3$). *Middle panel:* Distance modulus as a function of right ascension. *Bottom panel:* Galactocentric velocity as a function of right ascension. The black lines in all three panels show the approximate tracks for Sgr leading and trailing stream stars. Green circles indicate stars that lie inside all three regions (declination, distance and velocity) appropriate for Sgr stars. We find 8 BS stars associated with Sgr and one possible BHB star (if its classification as a BHB is incorrect). Three CN stars at RA $\sim$ 220 deg are likely associated with the Sgr leading arm. The remaining distant BHB and CN stars show no evidence for spatial or velocity clustering and we consider it unlikely that they all belong to a common substructure.

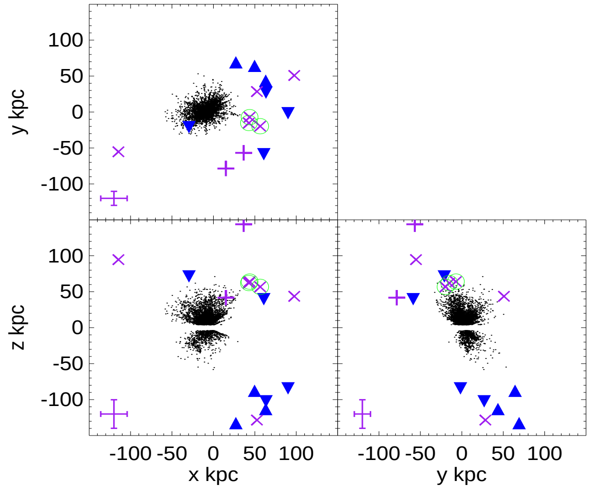

Figure 8. The x, y and z positions of our distant BHB (blue triangles) and CN (purple crosses) stellar halo stars. The stars with positive radial velocities ($v_{\rm GSR} > 0$) are indicated by blue triangles or purple crosses, while the stars with negative radial velocities ($v_{\rm GSR} < 0$) are indicated by the blue upside down triangles and the purple plus symbols. For comparison, we show the spatial distribution of the Xue et al. (2011) sample of BHB stars selected from SDSS. The green circles indicate the 3 CN stars that may belong to the Sgr leading arm. The uncertainty in the CN star coordinates is shown by the error bars in the bottom-left corner of every panel. The distance errors for the BHB stars are smaller than the symbol sizes. Our distant sample is sparsely distributed and shows no sign of belonging to a common substructure.

velocity space of the Sgr leading and trailing arms. The green circles indicate stars which coincide with the Sgr streams both in position, distance and velocity. We identify 8 BS stars that possibly belong to the Sgr stream. This is unsurprising given the distances of these stars (~ 50 kpc) and the fact that many of the SDSS overlaps coincide with this stellar halo stream (see shaded regions in the top panel of Fig. 7). We also identify one BHB star that may be associated with Sgr *if* we have classified it incorrectly. This star (85-TARG33) has an evidence ratio $K = 158$ based on BHB and BS star template fitting and a BHB model is still strongly favoured if the number ratio prior of BHB-to-BS stars is taken into account ($\tilde{K} = 30$). Thus, we still consider this a genuine distant BHB star. There are 3 CN stars that likely belong to the Sgr leading arm. While their distances are slightly too high, given the uncertainties, we still believe that they could possibly belong to the Sgr stream. We note that many of the halo carbon stars within $D < 100$ kpc have been identified as belonging to the Sgr stream (see e.g. Ibata et al. 2001), so it is unsurprising that some of our nearest CN stars in our sample may also belong to this overdensity.

In Fig. 8 we show the x, y and z positions of our distant BHB and CN stars. For comparison, we show the spatial distribution of the Xue et al. (2011) sample of BHB stars with distances $D < 60$ kpc. Our sample of distant stellar halo stars are distributed over a wide range of distances and sky area. In summary, whilst some BS (and CN) stars in our sample likely belong to a known stellar halo substructure, there is no evidence that our distant BHB and CN stars belong to a *common* overdensity.

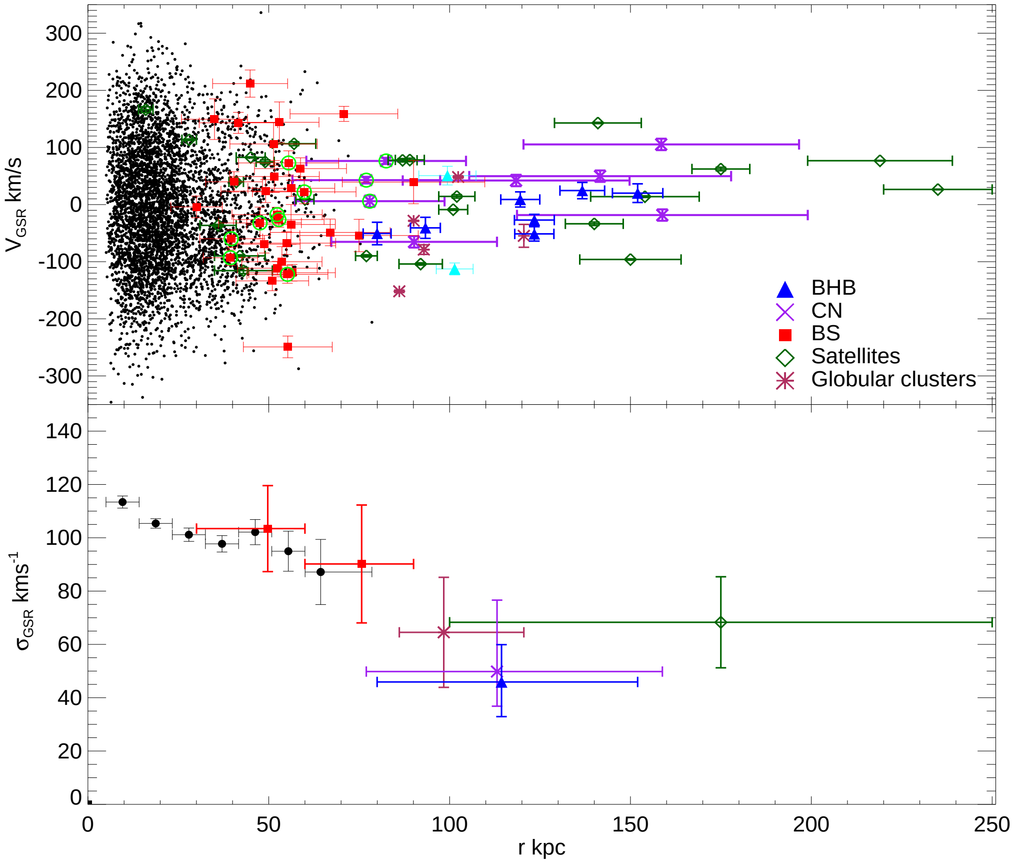

Figure 9. *Top panel:* Galactocentric velocity as a function of radius. The black points are BHB stars selected by Xue et al. (2011) from SDSS DR8. The red squares are BS stars. The blue triangles are BHB stars and the cyan triangles are 2 distant field BHBs classified by Clewley et al. (2005). The purple crosses are CN stars. The green circles indicate BS and CN stars that likely belong to the Sgr stream. The green diamonds are the Milky Way satellite galaxies (excluding Leo I at 250 kpc) and the red astericks are the distant Milky Way globular clusters. *Bottom panel:* The velocity dispersion profile of field halo stars. The colour coding for the different stellar populations is the same as the above panel. The migration of stars between the two BS star bins due to distance uncertainties is included in their velocity dispersion errors. The error in the velocity dispersion for the distant BHB stars includes the additional uncertainty of excluding/including borderline BHB/BS stars. We also incorporate the additional uncertainty of including/excluding possible Sgr stream members in the velocity dispersion of the CN stars.

5 VELOCITY DISPERSION PROFILE

In this section, we analyse the kinematics of our distant stellar halo sample. The top panel of Fig. 9 shows the Galactocentric velocities of stellar halo stars as a function of Galactocentric distance. The black points are the BHB spectroscopic sample compiled by Xue et al. (2011) from SDSS DR8; these stars probe out to $r \sim 60$ kpc. The red squares are our BS stars. The blue triangles are our 7 distant BHB stars. We also show the 2 distant (field) BHB stars identified by Clewley et al. (2005) with the cyan triangles. The purple crosses are our 8 distant CN type stars. The green circles indicate the BS and CN stars, which likely belong to the Sgr stream. We also show the (classical and ultra-faint) Milky Way satellite galaxies and the distant (beyond 80 kpc) Milky Way globular clusters by the green diamonds and maroon asterisks respectively. We note that there are now 31 tracers beyond 80 kpc. This is a significant improvement to the 10 tracers (5 globular clusters, 4 satellite galaxies and 1 halo star) used by Battaglia et al. (2005).

The bottom panel gives the velocity dispersion profile for stellar halo stars[3]. We also give the dispersion for satellite galaxies within $100 < r/\mathrm{kpc} < 250$ by the green error bar. We find the striking result that the velocity dispersion is *remarkably low at large distances*, dropping to $\sigma \sim 50 - 60$ km s^{-1} between $100 < r/\mathrm{kpc} < 150$. The outer parts of the stellar halo seemingly comprise a cold and tenuous veil. A less drastic decline, but still consistent within the errors, is seen in the satellite galaxies and globular clusters in this radial regime, as first noticed by Battaglia et al. (2005).

Owing to the small number statistics in the outermost bin for BHB stars ($\sim$ 7 stars), we consider the additional uncertainty in this measurement if borderline BHB/BS stars are included or excluded. In Fig. 10, we show Galactocentric velocity against the evidence ratio (K) of BHB versus BS template model fits (top panel) and the difference in Chi-square between the best-fitting BHB and BS models $(\Delta\chi^2)$ (bottom panel). We classify stars according to the evidence ratio with BHB stars have $K > 1$. However, BHBs

---

[3] **We note that when deriving the velocity dispersions, the velocity errors have been subtracted in quadrature**

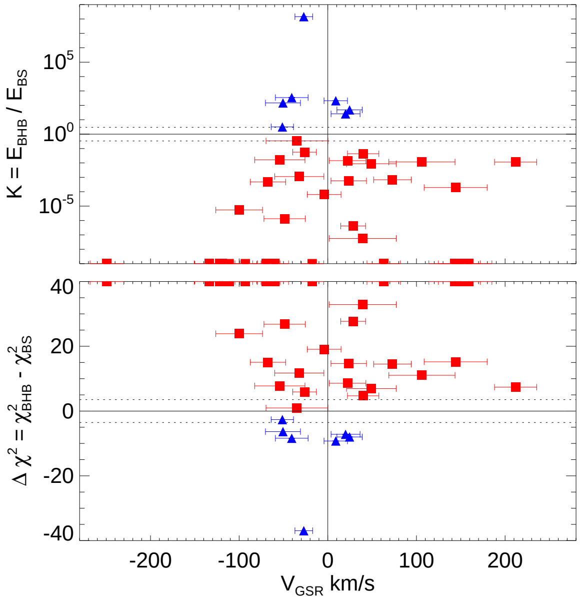

Figure 10. *Top panel:* Bayes factor as a function of Galactocentric radial velocity. Red squares and blue triangles denote BS and BHB stars respectively. The dotted lines at $K = 3$ and $K = 1/3$ indicate a 'substantial' strength of evidence favouring a BHB or BS model, respectively. BS stars with a very low Bayes factor ($< 10^{-9}$) are shown at the 10^{-9} level. *Bottom panel:* The difference between the minimum Chi-square BHB model and the minimum Chi-square BS model as a function of Galactocentric radial velocity. The dotted lines indicate 68% confidence boundaries (assuming 3 degrees of freedom). BS stars with $\Delta\chi^2 > 40$ are shown at the $\Delta\chi^2 = 40$ level.

with $1 < K < 3$ or BSs with $1/3 < K < 1$ do not *strongly* favour particular model templates. The top panel of Fig. 10 shows that there are two borderline cases (1 BHB, 1 BS). These stars have correspondingly small differences between the Chi-square values of their best fitting BHB and BS templates (see bottom panel). We consider the effect on our results if these borderline cases have been misclassified. This additional uncertainty (i.e. whether we classify BHB stars $K > 1/3, 1, 3$) is included in the uncertainty of the velocity dispersion in Fig. 9. We also note that the uncertainty on the CN star velocity dispersion takes into account the effect caused by the inclusion/exclusion of the 3 possible Sgr leading arm members. Thus, our results are robust to the treatment of borderline cases.

The observed cold outer stellar halo has implications for the total mass of our Galaxy, which we now compute using the tracer mass estimator of Watkins et al. (2010). We apply the estimator to distant stellar halo stars with $r > 50$ kpc. This distant sample comprises 144 BHB and BS stars between $50 - 90$ kpc and 17 BHB and CN stars between $80 - 160$ kpc. The Watkins et al. (2010) mass estimators assume that the tracer population has a scale-free density and moves in a scale-free potential in the region of interest. The total mass within the outermost tracer depends on 3 unknown parameters: the tracer density profile slope (α), the tracer velocity anisotropy ($\beta = 1 - \sigma_t^2/\sigma_r^2$) and the slope of the mass profile (γ). The mass within the outermost tracer ($r_{\rm out}$) is computed using equation 16 in Watkins et al. (2010)[4]:

$$M = \frac{C}{G}\langle v_r^2 r^\gamma \rangle, \quad C = (\gamma + \alpha - 2\beta)\, r_{\rm out}^{1-\gamma} \tag{5}$$

In this radial regime ($50 < r/\mathrm{kpc} < 150$), we can take $\gamma \approx 0.55$, which is appropriate for Navarro-Frenk-White (NFW; Navarro et al. 1996) type haloes beyond the scale radius, $r > r_s$ (see Watkins et al. 2010). We also consider isothermal ($\gamma = 0$) and Keplerian ($\gamma = 1$) halo models. We show the total mass as a function of the remaining unknown parameters in Fig. 11. We discard any models that are inconsistent (by more than 2σ) with the recent mass estimate by Deason et al. (2012) within 50 kpc: $M(50) = 4.2 \pm 0.4 \times 10^{11}$. We have checked that our mass estimates are not significantly affected by the inclusion/exclusion of borderline cases (i.e. misidentified BHB/BS stars and Sgr CN stars). The uncertainties due to the unknown tracer density fall-off and orbital properties dominate over observational errors and small number statistics.

The mass within 150 kpc ranges from $10^{11.5} - 10^{12.2} M_\odot$ depending on the adopted potential profile, tracer density fall-off and orbital structure. Massive haloes ($> 10^{12} M_\odot$) require an isothermal profile between 50-150 kpc and a tracer density profile that falls off very quickly ($\alpha > 5$), and/or tangentially biased tracer orbits ($\sigma_t^2/\sigma_r^2 > 1$). The latter possibility was advocated by Battaglia et al. (2005) to explain the apparent decline in velocity dispersion at large distances whilst Dehnen et al. (2006) advocated the former. The allowed range of masses for NFW ($M(150) = 6 - 8 \times 10^{11} M_\odot$) and Keplerian ($M(150) = 3.5 - 5 \times 10^{11} M_\odot$) models are all less than $10^{12} M_\odot$ over a large range of tracer properties.

6 DISCUSSION

6.1 Unrelaxed stars?

Commonly used mass estimators, such as those derived in Watkins et al. (2010), implicitly assume that the kinematic tracers are relaxed. How applicable is this assumption for the distant BHB stars in our sample? Recently, Deason et al. (2011b) showed that the stellar halo, as traced by BHB stars, is relatively smooth within $r < 50$ kpc. On the other hand, Bell et al. (2008) find a much lumpier stellar halo when traced by main-sequence turn-off stars. While BHB tracers seem to be the most relaxed of any stellar halo tracer, it is not easy to extrapolate the properties of the inner stellar halo to the outskirts. In fact, the much longer dynamical time scales at larger radii suggest that the outer reaches of the stellar halo are likely dominated by unrelaxed substructure. Can we then trust our dynamical mass estimators in this distant radial regime?

Wilkinson & Evans (1999) estimated how correlations in phase-space may effect mass estimates by considering the (somewhat extreme) case in which all their data lie along two streams. The authors found that mass is systematically underestimated by 20-50 per cent in this special case. More recently, Yencho et al. (2006) considered a more general case. They applied standard mass estimators to samples of tracers drawn from random realisations of galaxy haloes containing levels of substructure consistent with cur-

---

[4] Note that Watkins et al. (2010) label γ as the tracer density profile, and α as the slope of the mass profile. We use the opposite convention in this work

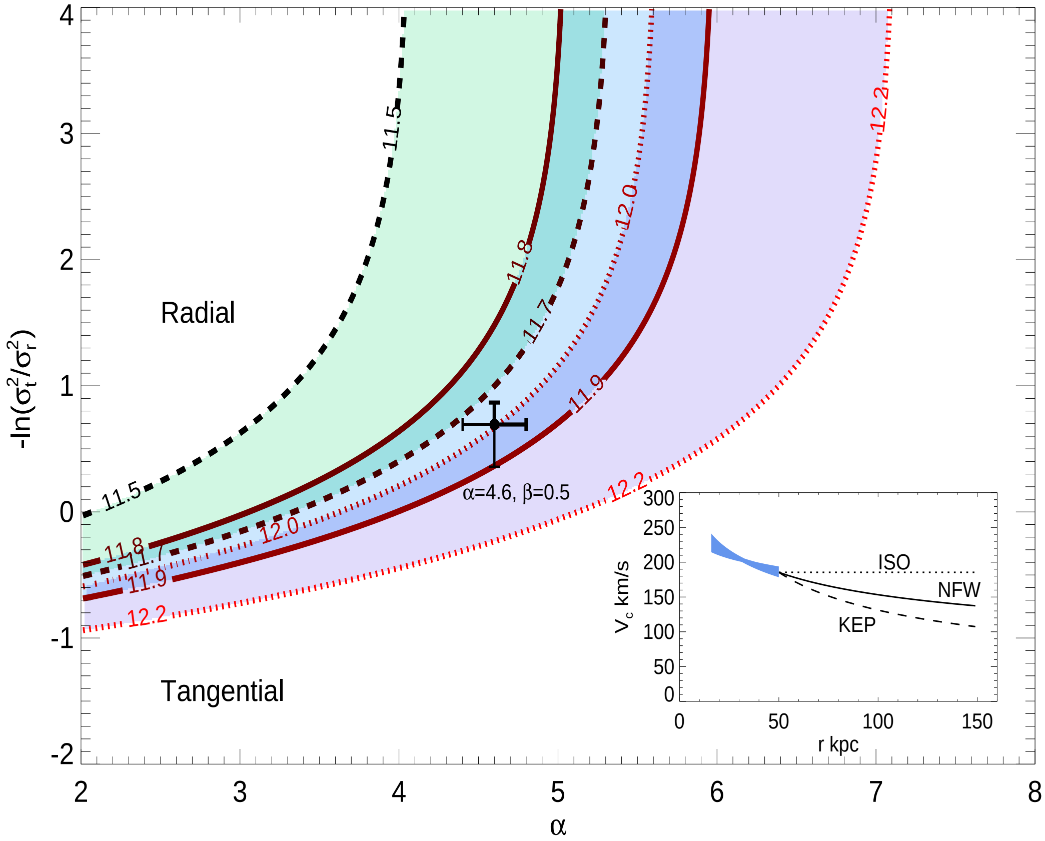

Figure 11. The contours show the estimated mass within 150 kpc for different potential profiles. The mass increases from black ($10^{11.5} M_\odot$) to red ($10^{12.2} M_\odot$). The solid contours are the masses for NFW haloes ($\gamma = 0.55$) and the dotted and dashed lines are for isothermal ($\gamma = 0$) and Keplerian ($\gamma = 1$) models respectively. Only models consistent with the recently measured mass within 50 kpc ($M(50) = 4.2 \pm 0.4 \times 10^{11}$; Deason et al. 2012) are shown. The allowed regions (for combinations of anisotropy, density and mass) for Keplerian, NFW and isothermal models are indicated by the green, blue and purple filled regions. The black error bar indicates the density profile and velocity anisotropy for tracers within 50 kpc (Deason et al. 2011b; Deason et al. 2012). If the tracers have moderate density fall-off ($\alpha < 5$) and radial orbits ($\sigma_t^2/\sigma_r^2 < 1$) then the mass within 150 kpc is less than $10^{12} M_\odot$. The inset panel shows the the circular velocity curve for example isothermal (dotted line), NFW (solid line) and Keplerian (dashed line) models. The blue shaded region indicates the circular velocity profile measured by Deason et al. (2012) within 50 kpc.

rent models of structure formation. The authors found distortions in their mass estimates at the level of 20 per cent.

A drop in radial velocity dispersion could signify that our distant stars belong to shell-like structures. Numerical simulations show that when a smaller galaxy collides with a larger system, a series of shell-like structures can form (e.g. Quinn 1984). The liberated stars from the collision follow very radial orbits with similar energies. A large enhancement of these stars at apocentre can thus build up into shell structures. The velocity structure in these shells is coincident with the systemic velocity of the host galaxy, with a very low dispersion. We quantify the effect of shells on our mass estimates by generating fake distributions of stars drawn from appropriate power-law distribution functions (cf. Watkins et al. 2010). We consider smoothly distributed tracers ($\alpha = 3.5$, between $50 < r/\mathrm{kpc} < 150$) with radially anisotropic orbits ($\beta = 0.5$) embedded in NFW type haloes ($\gamma = 0.55$). We then superimpose stars at large distances ($r > 80$ kpc) with low radial velocities (with $\sigma_r \sim 50$ km s^{-1}) onto this smooth distribution. The mass estimators used in the previous section (see eqn. 5) are then applied to this test data set, for which we assume α, γ and β are known. In our observational sample, 10 per cent of the stars are in the outer mass bin ($r > 80$ kpc). We ensure the same fraction of stars are in this outer mass bin when we estimate the mass of the fake data set. In Fig. 12, we show the results of this exercise, in which we vary the fraction of stars beyond $r = 80$ kpc that belong to shells from 0-100 per cent. We show three examples of halos with masses within 150 kpc of $1 \times 10^{12} M_\odot$ (solid red), $2 \times 10^{12} M_\odot$ (dashed blue) and $3 \times 10^{12} M_\odot$ (dot-dashed green) respectively. This simple calculation shows that the mass is underestimated by up to 10 per cent if *most* of the stars beyond 80 kpc belong to shells. A larger sample of stars beyond 80 kpc is needed to to test whether or not this drop in radial velocity dispersion is indeed caused by the presence of shells.

In summary, it is unlikely that substructure is strongly biasing our mass estimates within $r = 150$ kpc. Tidal streams are excluded by the the lack of phase-space correlation in our distant BHB and CN star sample. It seems reasonable to assume the presence of substructure at large radii introduces an additional uncertainty in our mass estimate at the level of 20 per cent. In particular, our mass estimates may be biased low (by up to 10 per cent) if many of our distant stars belong to shells. Even so, this is a negligible contribu-

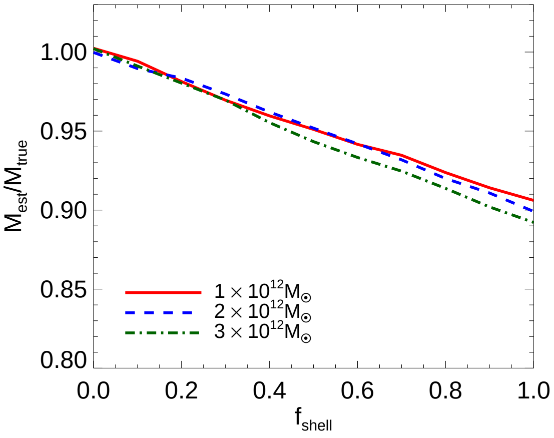

Figure 12. The bias in our mass estimates introduced by the presence of shells at large radii. We show examples of three different mass haloes ($1, 2, 3 \times 10^{12} M_\odot$) by the solid red, dashed blue and dot-dashed green lines, respectively. In each case, smoothly distributed tracers with density profile $\alpha = 3.5$ and radially anisotropic orbits ($\beta = 0.5$) are embedded in NFW-type haloes ($\gamma = 0.55$). When the mass estimator is applied we ensure that 10 per cent of the sample has $r > 80$ kpc, which is the same fraction as the observed sample (there are 17 stars (out of 161) beyond 80 kpc). A fraction of stars beyond 80 kpc ($f_{\rm shell}$) are given a low radial velocity distribution (with $\sigma_r \approx 50$ km s^{-1}) to mimic the presence of shells superimposed on a smooth distribution of stars. The presence of shells at large distances causes an underestimate in the mass by up to 10 per cent.

tion compared to the systematic uncertainty in the tracer properties such as density and anisotropy.

6.2 Tangential anisotropy and/or rapid tracer density fall-off?

The cold radial velocity dispersion at large radii may be caused by the dominance of tangential motions. But is there physical justification for this picture? Current theories predict that the stripped stellar material from accreted satellite galaxies make up the bulk of the stellar halo (e.g. Bullock & Johnston 2005; Cooper et al. 2010). Recently, other formation scenarios have been suggested for the inner stellar halo (i.e. *in situ* formation, see e.g. Zolotov et al. 2009; Font et al. 2011), but accretion seems the only likely scenario in the outer regions. Model stellar haloes built up from the accretion of satellites predict *strongly radial orbits* (e.g. Diemand et al. 2007; Sales et al. 2007). Observational constraints from the solar neighbourhood and inner (< 50 kpc) stellar halo find radially biased orbits ($\sigma_t^2/\sigma_r^2 \sim 0.5$, e.g Smith et al. 2009a; Deason et al. 2012) and thus seem to concur with theoretical predictions. The fact that the radial anisotropy is only expected to increase with radius further contradicts the notion of tangentially biased orbits in the radial regime $100 < r/{\rm kpc} < 150$. Thus, given current observational constraints and theoretical predictions, it is unlikely that tangential anisotropy can explain the presence of such a cold radial velocity dispersion.

Another possibility is that the density profile of the stellar halo falls sharply at large distances. While the stellar halo density profile within 50 kpc has been studied extensively (e.g. Bell et al. 2008; Jurić et al. 2008; Deason et al. 2011b; Sesar et al. 2011), constraints at larger radii are rare. In the radial range of our distant stars ($100 < r/{\rm kpc} < 150$), we are probing the tail of the stellar distribution and it is reasonable to assume that the stellar density may be falling off very rapidly. In fact, Dehnen et al. (2006) showed that a sharp decline in velocity dispersion can be produced by radially anisotropic ($\sigma_t^2/\sigma_r^2 \sim 0.5$) tracers with a truncated density distribution ($r_t = 160$ kpc) embedded within a $1.5 \times 10^{12} M_\odot$ halo. Does such a cold velocity dispersion then signify that we are probing the edge of the stellar halo? Spectroscopic programmes targeting halo stars beyond 150 kpc will be vital in order to address this point.

It is important to bear in mind that a low (albeit less extreme) velocity dispersion is also seen in the satellite galaxy population. There is no requirement that the stellar halo stars and satellite galaxies should share a similar density profile and/or velocity anisotropy. In fact, the distribution of satellite galaxies in our own Galaxy and M31 is believed to be much shallower than stellar halo stars (e.g. Watkins et al. 2010). Furthermore, the proper motions of the classical Milky Way satellites suggest that they have tangentially biased orbits, whereas numerical simulations predict that stellar halo stars have strongly radial orbits. The fact that *both* of these halo populations have a cold radial velocity dispersion beyond 100 kpc suggests that there is a common cause, namely part (if not all) of the decline must be related to the mass profile.

6.3 A low mass, high concentration halo?

It is clear from Fig. 11 that, discounting a stellar population with tangential velocity anisotropy ($\sigma_t^2/\sigma_r^2 > 1$) and/or a rapid decline in density between $50 - 150$ kpc ($\alpha > 5$), the mass within 150 kpc is less than $10^{12} M_\odot$ and probably lies in the range $M(< 150{\rm kpc}) = (5 - 10) \times 10^{11} M_\odot$. In particular, if we extrapolate measurements of tracer density and anisotropy within 50 kpc to 150 kpc, namely $\alpha \sim 4.6$ and $\beta = 0.5$, we find that $M(< 150{\rm kpc}) \sim 7 \times 10^{11} M_\odot$ (assuming an NFW halo with $\gamma = 0.55$). Given that the total mass within 50 kpc is $\sim 4 \times 10^{11} M_\odot$, our results suggest that *there may be little mass between 50 and 150 kpc*. Is most of the dark matter in our Galaxy therefore highly concentrated in the centre? Deason et al. (2012) recently found that the dark matter profile of our Galaxy within 50 kpc is highly concentrated ($c_{\rm vir} \sim 20$). Our results presented here for the outer halo are in agreement with the deductions from the inner halo.

Our findings also agree with several other recent studies suggesting that the Milky Way may be less massive than previously thought (e.g. Battaglia et al. 2005; Smith et al. 2007; Xue et al. 2008). This has important repercussions for numerical simulations attempting to reproduce Milky Way type galaxies, where often the biggest scatter in halo properties comes from their total masses. For example, Wang et al. (2012) recently showed that the number of massive Milky Way subhaloes strongly depends on the virial mass of the halo (see also Vera-Ciro et al. 2012). The lack of massive satellites in our Galaxy (the ‘missing massive satellites’ problem, Boylan-Kolchin et al. 2012) could simply indicate a less massive halo ($M_{200} < 10^{12} M_\odot$). However, a low halo mass may prove problematic for semi-analytic models which attempt to match the observed Tully-Fisher relation and galaxy stellar mass function (e.g. Cole et al. 2000; Croton et al. 2006). Generally, agreement with observations requires that the virial velocity ($V_{200} \sim 150$ km s^{-1} for $M_{200} \sim 10^{12} M_\odot$) and rotation speed of the galaxy are comparable (i.e. $V_{200} \sim V_{\rm rot}$). Thus, a rotation speed of 220-250 km s^{-1} for the Milky Way disc and a low halo mass is at odds with these semi-analytic models.

A low mass Milky Way halo also has implications regarding the origin of several satellite galaxies. Leo I would almost certainly be unbound with a distance of 250 kpc and a substantial radial velocity of $V_{\rm GSR} \sim 180$ km s^{-1}. In addition, recent proper motion measurements of the Small and Large Magellanic Clouds (SMC/LMC) (Kallivayalil et al. 2006a; Kallivayalil et al. 2006b) suggest that the total velocities of these clouds approach the escape speed of the Milky Way. Besla et al. (2007) showed that under the assumption of a Milky Way with virial mass $M_{\rm vir} \sim 10^{12} M_{\odot}$, the LMC and SMC are on their first passage about the Milky Way. The current results seem to increase the likelihood that the SMC/LMC are unbound.

7 CONCLUSIONS

We have built a sample of distant stellar halo stars beyond $D > 80$ kpc with measured radial velocities. Our sample consists of relatively old BHB stars and intermediate age AGB stars. We target BHB stars in the magnitude range $20 < g < 22$ using multi-epoch SDSS photometry. Using follow-up spectroscopic observations with the VLT-FORS2 instrument we obtained radial velocities for 38 A-type stars. We distinguish between BHB and BS stars by fitting noise-free BHB and BS templates built from high S/N SDSS spectra. Our sample comprises 7 BHB stars in the radial range $80 < r_{\rm BHB}/{\rm kpc} < 150$ and 31 less distant BS stars with $30 < r_{\rm BS}/{\rm kpc} < 90$. In addition, a sample of 4 distant cool carbon stars with measured radial velocities was compiled from the literature. We measured radial velocities for an additional 4 carbon stars using the WHT-ISIS instrument. Our 8 carbon stars span a distance range $80 < r_{\rm CN} < 160$ kpc and are a useful, complementary sample to the older BHB population. We summarise our conclusions as follows:

(1) The velocity dispersion of the distant BHB and CN stars is surprisingly low with $\sigma_{\rm GSR} \sim 50-60$ km s^{-1}. The outer parts of the stellar halo may be likened to a cold veil.

(2) Although, a significant number of the BS and CN stars (8 and 3 respectively) are coincident with the Sagittarius (Sgr) stream, our sample of BHB stars (and the remaining CN stars) are widely distributed across the sky and show no evidence that they belong to a common substructure. However, such a low radial velocity dispersion could be caused by the presence of shells at large radii.

(3) The observed low velocity dispersion profile is robust to the inclusion/exclusion of borderline BHB candidates and CN star Sgr members. The velocity dispersion of satellite galaxies in a similar radial range ($100 < r/{\rm kpc} < 250$) is also low, $\sigma_{\rm GSR} \sim 70$ km s^{-1}. Battaglia et al. (2005) first noted this decline in radial velocity dispersion for distant satellite galaxy and globular cluster tracers. We now confirm that a similar, if not more extreme, cold velocity dispersion is seen in distant stellar halo stars.

(4) The implications for the total mass of our Galaxy depends on the (unknown) density profile and velocity anisotropy of the tracer population. However, discounting a stellar population with a tangential velocity bias ($\sigma_t^2/\sigma_r^2 > 1$) and/or a rapid tracer density fall-off ($\alpha > 5$) between $50-150$ kpc, we find that the total mass within 150 kpc is less than $10^{12} M_{\odot}$ and probably lies in the range $(5-10) \times 10^{11} M_{\odot}$. Our results thus suggest that the total mass of our Galaxy may be lower than previously thought.

In this study, we have expanded the sample of tracers out to $r \sim 150$ kpc — near the edge of the stellar halo. Larger samples of tracers are needed to add further statistical weight to our results. We intend to address this issue over the next few years by combining deep and wide photometric surveys with 4-10m class telescopes equipped with moderate/high resolution spectrographs. Ultimately, even with a much larger number of halo tracers, the uncertainty surrounding the tracer velocity anisotropy and density needs to be addressed. Over the next few years it will become vital to *measure* these tracer properties rather than to infer them.

ACKNOWLEDGEMENTS

AJD thanks the Science and Technology Facilities Council (STFC) for the award of a studentship. VB acknowledges financial support from the Royal Society. S.K. acknowledges financial support from the STFC. RC is supported by a Research Fellowship at Peterhouse College, Cambridge. JP acknowledges support from the Ramón y Cajal Program as well as by the Spanish grant AYA2010-17631 awarded by the Ministerio of Economía y Competitividad. CFPL is currently supported by the Marie Curie Initial Training Network CosmoComp (PITN-GA-2009-238356. MF acknowledges funding through FONDECYT project No. 1095092 and BASAL. MGW is currently supported by NASA through Hubble Fellowship grant HST-HF-51283.01-A, awarded by the Space Telescope Science Institute, which is operated by the Association of Universities for Research in Astronomy, Inc., for NASA, under contract NAS5-26555. EO was partially supported by NSF grant AST0807498. It is a pleasure to thank Mike Irwin and Paul Hewett for useful comments and advice. We also thank an anonymous referee for useful comments.

REFERENCES

Battaglia G., Helmi A., Morrison H., Harding P., Olszewski E. W., Mateo M., Freeman K. C., Norris J., Shectman S. A., 2005, MNRAS, 364, 433
Bell E. F., et al., 2008, ApJ, 680, 295
Belokurov V., et al., 2007, ApJ, 654, 897
Besla G., Kallivayalil N., Hernquist L., Robertson B., Cox T. J., van der Marel R. P., Alcock C., 2007, ApJ, 668, 949
Bovy J., Hogg D. W., Rix H., 2009, ApJ, 704, 1704
Boylan-Kolchin M., Bullock J. S., Kaplinghat M., 2012, MNRAS, p. 2657
Brown W. R., Geller M. J., Kenyon S. J., Diaferio A., 2010, AJ, 139, 59
Bullock J. S., Johnston K. V., 2005, ApJ, 635, 931
Clewley L., Warren S. J., Hewett P. C., Norris J. E., Peterson R. C., Evans N. W., 2002, MNRAS, 337, 87
Clewley L., Warren S. J., Hewett P. C., Norris J. E., Wilkinson M. I., Evans N. W., 2005, MNRAS, 362, 349
Cole S., Lacey C. G., Baugh C. M., Frenk C. S., 2000, MNRAS, 319, 168
Cooper A. P., et al., 2010, MNRAS, 406, 744
Croton D. J., et al., 2006, MNRAS, 365, 11
Deason A. J., Belokurov V., Evans N. W., 2011a, MNRAS, 411, 1480
Deason A. J., Belokurov V., Evans N. W., 2011b, MNRAS, 416, 2903
Deason A. J., Belokurov V., Evans N. W., An J. H., 2012, MNRAS in press, arXiv:1204.5189
Dehnen W., McLaughlin D. E., Sachania J., 2006, MNRAS, 369, 1688
Diemand J., Kuhlen M., Madau P., 2007, ApJ, 667, 859

Font A. S., McCarthy I. G., Crain R. A., Theuns T., Schaye J., Wiersma R. P. C., Dalla Vecchia C., 2011, MNRAS, 416, 2802

Gnedin O. Y., Brown W. R., Geller M. J., Kenyon S. J., 2010, ApJ, 720, L108

Ibata R., Lewis G. F., Irwin M., Totten E., Quinn T., 2001, ApJ, 551, 294

Jeffreys H., 1961, Theory of Probability, third edn. Oxford Univ. Press

Jurić M., et al., 2008, ApJ, 673, 864

Kallivayalil N., van der Marel R. P., Alcock C., 2006b, ApJ, 652, 1213

Kallivayalil N., van der Marel R. P., Alcock C., Axelrod T., Cook K. H., Drake A. J., Geha M., 2006a, ApJ, 638, 772

MacKay D., 2003, Information Theory, Inference, and Learning Algorithms. Cambridge, UK, Cambridge University Press, 2003, 640 p.

Markwardt C. B., 2009, in D. A. Bohlender, D. Durand, & P. Dowler ed., Astronomical Data Analysis Software and Systems XVIII Vol. 411 of ASP Conf. Ser.. p. 251

Mauron N., 2008, A&A, 482, 151

Mauron N., Azzopardi M., Gigoyan K., Kendall T. R., 2004, A&A, 418, 77

Mauron N., Kendall T. R., Gigoyan K., 2005, A&A, 438, 867

McMillan P. J., 2011, MNRAS, 414, 2446

Navarro J. F., Frenk C. S., White S. D. M., 1996, ApJ, 462, 563

Quinn P. J., 1984, ApJ, 279, 596

Reid M. J., et al., 2009, ApJ, 700, 137

Rohlfs K., Kreitschmann J., 1988, A&A, 201, 51

Sales L. V., Navarro J. F., Abadi M. G., Steinmetz M., 2007, MNRAS, 379, 1464

Samurović S., Lalović A., 2011, A&A, 531, A82

Schönrich R., Binney J., Dehnen W., 2010, MNRAS, pp 149–+

Sersic J. L., 1968, Atlas de galaxias australes. Observatorio Astronomico, Cordoba

Sesar B., Jurić M., Ivezić Ž., 2011, ApJ, 731, 4

Sirko E., et al., 2004, AJ, 127, 899

Smith M. C., et al., 2007, MNRAS, 379, 755

Smith M. C., et al., 2009a, MNRAS, 399, 1223

Totten E. J., Irwin M. J., 1998, MNRAS, 294, 1

Totten E. J., Irwin M. J., Whitelock P. A., 2000, MNRAS, 314, 630

Vera-Ciro C. A., Helmi A., Starkenburg E., Breddels M. A., 2012, MNRAS submitted, arXiv:1202.6061

Wang J., Frenk C. S., Navarro J. F., Gao L., 2012, MNRAS submitted, arXiv:1203.4097

Watkins L. L., Evans N. W., An J. H., 2010, MNRAS, 406, 264

Wilkinson M. I., Evans N. W., 1999, MNRAS, 310, 645

Xue X. X., et al., 2008, ApJ, 684, 1143

Xue X. X., et al., 2011, ApJ, 738, 79

Yencho B. M., Johnston K. V., Bullock J. S., Rhode K. L., 2006, ApJ, 643, 154

Zolotov A., Willman B., Brooks A. M., Governato F., Brook C. B., Hogg D. W., Quinn T., Stinson G., 2009, ApJ, 702, 1058